

Structure and Physical Properties of Molecule-Based Magnets Including Transition Metal Complexes of Crown Thioethers

Junichi Nishijo, Akira Miyazaki, and Toshiaki Enoki*

Department of Chemistry, Graduate School of Science and Engineering, Tokyo Institute of Technology, Ookayama, Meguro-ku, Tokyo 152-8551

Received August 1, 2003; E-mail: tenoki@chem.titech.ac.jp

A new series of molecule-based magnets, including crown thioether (9S3 = 1,4,7-trithiacyclononane) complexes of transition metals (Ni, Co, Cu), are presented. TCNQ salts $[M(9S3)_2](TCNQ)_2$ (M = Ni, Co) are one-dimensional (1D), antiferromagnetic (AF) complexes with an intra-chain interaction $J = -3.9$ K and -1.3 K for M = Ni and Co, respectively, despite its long intermolecular distance, for which the large spin density on the sulfur atom in the magnetic $[M(9S3)_2]^{2+}$ cation is responsible. The mixed valence salt $[M(9S3)_2](TCNQ)_3$ (M = Ni, Co) is a paramagnetic semiconductor. 1D AF magnet $[Cu(9S3)Br_2]$ does not undergo any magnetic transition because of the weak inter-chain interaction. Substituting a very small amount (~5%) of Cu with Ni causes a structural change. The change decreases the distances of inter-chain S–S contacts, resulting in the generation of an AF transition at $T_N = 4.5$ K. $[M(9S3)_2][Ni(bdt)_2]_2$ (M = Ni, Co; bdt = 1,2-benzenedithiolato) are weak-ferromagnets with $T_N = 6.2$ K and 2.6 K for M = Ni and Co, respectively. In the crystals, $[M(9S3)_2]^{2+}$–$[Ni(bdt)_2]^-$ alternate chains and $[Ni(bdt)_2]^-$ uniform chains coexist. The appearance of weak-ferromagnetism is associated with a competition between two kinds of inter-chain AF interactions between $[M(9S3)_2]^{2+}$–$[Ni(bdt)_2]^-$ alternate chains, where the stronger one is an indirect inter-chain interaction through $[Ni(bdt)_2]^-$ uniform chains, while the weaker is a direct inter-chain interaction.

Molecule-based magnets, especially transition metal complexes, have been intensively investigated in recent years from the view point of applications and basic science interests in their low dimensionality, quantum mechanical features and interplay between electron transport and magnetism.[1–12] One of the most important issues in designing molecule-based magnets is to make a magnetic interaction network between constituent molecules as building blocks. From the lesson of traditional transition metal magnets, conduction electrons, which can mediate interactions between magnetic sites, are a promising tool in making these networks. Actually, strong magnetic interactions in iron and manganese oxides are the consequence of conduction electron-mediated exchange interactions. Based on this scheme, molecule-based magnetic conductors are designed to mimic such traditional magnets.[9–16] In the most popular molecule-based magnetic conductors developed so far, transition metal magnetic anions containing halogen atoms at ligand sites are incorporated into tetrathiafulvalene (TTF) type charge transfer complexes.[9–12] In these salts, conduction π-electrons of TTF donors can interact with the localized magnetic moments of anions (π–d interaction) through the inter-molecular atomic contact between the sulfur atom of the donor and the halogen sites of the anions. However, π–d interactions are usually very weak in these systems because the spin density at halogen atoms of anions is quite small. To solve this problem, transition metal complexes containing sulfur atoms at ligand sites are used. Indeed, the π-acidity of sulfur-containing ligands, which produce back donation from the central metal atom, increases the spin density at the sulfur atom of the ligands. Furthermore, the large atomic orbitals of sulfur atoms can also enhance the π–d interactions through S–S contacts between donor and anion. The idea of inter-molecular S–S atomic contact is also expected to be applicable in designing a strong interaction network[17] in insulating molecule-based magnets where superexchange paths with S–S bridges work in place of π–d interactions.

Under the impetus mentioned above, we have been surveying sulfur-containing magnetic building blocks which can effectively work in the architecture of molecule-based magnets. Though no attention has yet been paid to crown thioethers in designing magnets, the π-acidity of crown thioethers[18,19] is suitable for building molecule-based magnets as it contributes to forming an extended electronic structure, which is inferable to enhancing magnetic interactions. In the present paper, we report a new class of molecule-based magnets with transition metal complexes of crown thioethers having sulfur atoms as the main ingredient. 9S3 = 1,4,7-trithiacyclononane, the crown thioether ligand we employ, is well known and a target of particular focus in the crown thioether area.[20,21] As counter anions or acceptors to these cations, we used TCNQ (= 7,7,8,8-tetracyanoquinodimethane), Br^-, $[Ni(dmit)_2]^-$ (dmit = isotrithionedithiolato), $[Ni(mnt)_2]^-$ (mnt = maleonitrile), and $[Ni(bdt)_2]^-$ (bdt = 1,2-benzenedithiolato) molecules. TCNQ is a well known acceptor, charge transfer salts of which frequently produce high conductive materials.[22–24] Br^- anions, which are small, can reduce the distances between cations due to the absence of steric hindrance. Therefore, it is expected that a strong interaction between crown thioether complexes will be produced. $[Ni(dmit)_2]^-$, $[Ni(mnt)_2]^-$, and $[Ni(bdt)_2]^-$ molecules are dithiolate planar complexes which also contain sulfur atoms. As a result, not only strong cation–cation, but also cation–anion interactions are expected through the mediation of

Published on the web April 2, 2004; DOI 10.1246/bcsj.77.715

intermolecular S–S contacts.

1. Experimental

1.1 Preparation. $[M(9S3)_2](BF_4)_2$ (M = Ni, Co, and Cu), *n*-$Bu_4N[Ni(dmit)_2]$, *n*-$Bu_4N[Ni(mnt)_2]$, and *n*-$Bu_4N[Ni(bdt)_2]$ were prepared according to the literature.[25–28]

$[Ni(9S3)_2](TCNQ)_2$ (**1**), $[Co(9S3)_2](TCNQ)_2$ (**2**), $[Ni(9S3)_2](TCNQ)_3$ (**3**), and $[Co(9S3)_2](TCNQ)_3$ (**4**). Single crystals of **1** and **3** were prepared using the diffusion method at $T = 45$ °C. In this method, we used an H-shape glass tube containing 50 mg of $[Ni(9S3)_2](BF_4)_2$ and 50 mg of Li-TCNQ in each side of the H-tube, and 30 mL of acetonitrile was used as the solvent. After two weeks, red triangular prism crystals of **1** and black plate crystals of **3** were grown at the midpoint of the H-tube. The same method with $[Co(9S3)_2](BF_4)_2$ at 45 °C and 5 °C gives a powder of **2** and **4**, respectively. The $[Cu(9S3)_2]^{2+}$ salt of TCNQ was not obtained by using $[Cu(9S3)_2](BF_4)_2$. Typical crystal size was $0.6 \times 0.6 \times 2$ mm^3 for **1** and $3 \times 3 \times 0.2$ mm^3 for **3**. Found for **1**: C, 52.07; H, 3.71; N, 13.68; S, 23.16%. Calcd for **1**: C, 52.23; H, 3.90; N, 13.54; S, 23.24%. Found for **2**: C, 52.31; H, 3.97; N, 13.80; S, 22.97%. Calcd for **2**: C, 52.22; H, 3.90; N, 13.53; S, 23.24%. Found for **3**: C, 55.58; H, 3.28; N, 16.21; S, 18.34%. Calcd for **3**: C, 55.87; H, 3.52; N, 16.29; S, 18.64%. Found for **4**: C, 55.91; H, 3.53; N, 16.17; S, 18.82%. Calcd for **4**: C, 55.85; H, 3.52; N, 16.28; S, 18.64%.

$[Cu(9S3)Br_2]$ (**5**) and $[Cu_{1-x}Ni_x(9S3)Br_2]$ ($x \sim 0.05$) (**6**). Single crystals were prepared using the diffusion method at $T = 5$ °C in 30 mL of acetonitrile solution. Single crystals of **5** slowly grew from 30 mg of $[Cu(9S3)_2](BF_4)_2$ and 30 mg of $CuBr_2$ over five weeks, and single crystals of **6** grew from 30 mg of $[Cu(9S3)_2](BF_4)_2$ and 50 mg of $NiBr_2$ in one week. The ratio of Cu to Ni of **6** was roughly estimated by EDAX analysis. The typical crystal size was $1.5 \times 1 \times 0.1$ mm^3 for **5** and $2.2 \times 1.5 \times 0.2$ mm^3 for **6**. Found for **5**: C, 18.02; H, 3.31; S, 23.59%. Calcd for **5**: C, 17.85; H, 3.00; S, 23.83%. Found for **6**: C, 17.79; H, 2.92; S, 23.91%. Calcd for **6**: C, 17.86; H, 3.00; S, 23.84%. We could not obtained $[Ni(9S3)Br_2]$ from $[Ni(9S3)_2](BF_4)_2$ and $NiBr_2$, which may be due to the stronger coordination bond between Ni^{2+} and 9S3 than that between Cu^{2+} and 9S3, inferred from metal-sulfur atomic distances.[25]

$[Ni(9S3)_2][Ni(bdt)_2]_2$ (**7**) and $[Co(9S3)_2][Ni(bdt)_2]_2$ (**8**).[29] A 50 mL acetonitrile solution of 50 mg $[M(9S3)_2](BF_4)_2$ was added to a 50 mL acetonitrile solution of 50 mg *n*-$Bu_4N[Ni(bdt)_2]$ at room temperature, and was slowly cooled to 0 °C. After standing for 4 h at 0 °C, black elongated plate crystals of **7** or **8** were obtained. The $[Cu(9S3)_2]^{2+}$ analogue of **7** was not obtained by using $[Cu(9S3)_2](BF_4)_2$. The typical crystal size was $3 \times 1 \times 0.1$ mm^3 and $1.4 \times 0.8 \times 0.03$ mm^3 for **7** and **8**, respectively. Found for **7**: C, 39.44; H, 3.32; S, 41.07%. Calcd for **7**: C, 39.39; H, 3.67; S, 40.90%. Found for **8**: C, 39.17; H, 3.42; S, 40.65%. Calcd for **8**: C, 39.38; H, 3.67; S, 40.89%.

It should be noted that neither $[Ni(dmit)_2]^-$ nor $[Ni(mnt)_2]^-$ salts of crown thioether complexes were successfully obtained.

1.2 X-ray Crystallography. The crystal structures of **1**, **3**, **5**, **6**, **7**, and **8** were determined by single crystal X-ray diffraction with a Rigaku AFC-7R four-circle diffractometer at 293 K, using Mo Kα radiation ($\lambda = 0.71069$ Å), where a suitable crystal was mounted on a glass fiber. The structures were solved using direct methods (SHELXS-86),[30] then refined with a full-matrix least-squares method (SHELXL-93).[31] An absorption correction based on a Ψ-scan was introduced. All non-hydrogen atoms were refined anisotropically, while hydrogen atoms were placed in their calculated positions and refined by the riding model. We used crystals of **1** (triangular prism, red, $0.2 \times 0.2 \times 0.5$ mm^3), **3** (plate, black, $0.5 \times 0.5 \times 0.1$ mm^3), **5** (plate, black, $0.2 \times 0.1 \times 0.05$ mm^3), **6** (plate, black, $0.4 \times 0.3 \times 0.1$ mm^3), **7** (elongated plate, black, $0.7 \times 0.2 \times 0.1$ mm^3) and **8** (elongated plate, black, $0.5 \times 0.2 \times 0.03$ mm^3) suitable for structural determinations. Crystallographic data for **1**, **3**, **5**, **6**, **7**, and **8** are summarized in Table 1. Crystals of **2** and **4** were confirmed to be isostructural to those of **1** and **3**, respectively, from the X-ray powder diffraction pattern. Crystallographic data have been deposited at the CCDC, 12 Union Road, Cambridge CB12 1EZ, UK and copies can be obtained on request, free of

Table 1. Crystallographic Data

	1	**3**	**5**	**6**	**7**	**8**
Temp/K	293(5)	293(5)	293(5)	293(5)	293(5)	293(5)
Formula	$C_{36}H_{32}N_8Ni_1S_6$	$C_{48}H_{36}N_{12}Ni_1S_6$	$C_6H_{12}Br_2Cu_1S_3$	$C_6H_{12}Br_2Cu_{1-x}Ni_xS_3$ ($x \sim 0.05$)	$C_{36}H_{40}Ni_3S_{14}$	$C_{36}H_{40}Co_1Ni_2S_{14}$
fw	827.77	1031.98	403.71	403.47	1097.72	1097.96
Crystal system	triclinic	triclinic	orthorhombic	monoclinic	triclinic	triclinic
Space group	$P\bar{1}$	$P\bar{1}$	$P2_12_12_1$	$P2_1/a$	$P\bar{1}$	$P\bar{1}$
a/Å	9.319(9)	10.418(3)	11.016(5)	14.000(9)	11.6629(19)	11.711(3)
b/Å	11.555(9)	14.535(4)	13.702(16)	10.919(6)	12.9372(11)	12.8406(16)
c/Å	8.627(9)	7.761(3)	7.633(3)	7.6261(19)	7.778(2)	7.7989(13)
α/deg	99.69(8)	93.04(3)	90	90	93.859(13)	92.682(12)
β/deg	95.86(11)	95.48(3)	90	104.18(4)	106.154(17)	107.022(17)
γ/deg	80.25(7)	92.38(2)	90	90	95.185(10)	95.400(15)
V/Å^3	899.9(14)	1167.0(6)	1152.1(15)	1130.3(10)	1117.4(4)	1113.0(4)
Z	1	1	4	4	1	1
Reflections collected ($2\theta < 55°$)	1736	4759	2088	2106	5167	4149
Reflections unique	1631	4325	1522	1660	4018	3141
R_1 for all data	0.0880	0.0460	0.0417	0.0557	0.0518	0.0426
wR_2 for all data	0.2266	0.1351	0.1008	0.1406	0.1156	0.0962

$R_1 = \Sigma(||F_0| - |F_C||)/\Sigma|F_0|$, $wR_2 = [\Sigma w(|F_0|^2 - |F_C|^2)^2/\Sigma w(|F_0|^2)^2]^{1/2}$.

charge, by quoting the publication citation and the deposition numbers 224684–224687 (for **1**, **3**, **5**, and **6**), 198892 and 198893 (for **7** and **8**).

1.3 Physical Measurements. Electrical conductivities of single crystals were measured using a two probe method for **1**, **3**, **5**, **6**, **7**, and **8**, whose crystal sizes were $0.2 \times 0.2 \times 0.4$ mm^3, $0.6 \times 0.3 \times 0.05$ mm^3, $0.3 \times 0.2 \times 0.1$ mm^3, $0.3 \times 0.2 \times 0.05$ mm^3, $0.6 \times 0.3 \times 0.1$ mm^3 and $0.4 \times 0.2 \times 0.05$ mm^3, respectively. Magnetic susceptibilities were measured by using a Quantum-Design MPMS-5 SQUID magnetometer for an assembly of aligned single crystals (**1**, **3**, **5**, and **6**), a packet of powder sample (**2**, **4**) whose typical weight was 1 to 1.5 mg, or one single crystalline sample (**7**, **8**) whose size and weight were $1.6 \times 0.4 \times 0.1$ mm^3 and 0.1 mg for **7** and $1.2 \times 0.4 \times 0.1$ mm^3 and 0.08 mg for **8**, respectively. The AC-susceptibility of **7** and **8** was measured using a Quantum-Design MPMS-XL SQUID magnetometer with an AC option for an assembly of aligned single crystals whose total weight was about 5 mg. The magnetic susceptibilities shown below were obtained after the subtraction of the core diamagnetic contributions from the observed susceptibilities.

2. Results and Discussion

2.1 Crystal Structures. 2.1.1 $[M(9S3)_2](TCNQ)_2$ (M = Ni (1), Co (2)) and $[M(9S3)_2](TCNQ)_3$ (M = Ni (3), Co (4)): The crystal structures of **1** and **3** are shown in Fig. 1a and 1b, respectively. The structures are similar to $[M([9]aneN_3)_2](TCNQ)_n$ (M = Ni, Cu, $n = 1, 2$, [9]aneN$_3$ = 1,4,7-triazacyclononane).[32] In crystal **1**, $TCNQ^-$ anions form non-magnetic dimers with a large intra-dimer overlap integral[33] ($= 2.64 \times 10^{-2}$), which are well separated from each other by the hindrance of $[Ni(9S3)_2]^{2+}$ cations, as confirmed by quite small inter-dimer overlap integrals ($\sim$0). $[Ni(9S3)_2]^{2+}$ cations form one-dimensional (1D) chains elongated parallel to the *c*-axis with an inter-molecular S–S contact of $r = 3.838(6)$ Å, which is slightly longer than the sum of the van der Waals radii of sulfur atoms (3.7 Å). Crystal **3** forms TCNQ trimers, which are also non-magnetic with two electrons stabilized in the singlet state, a result of large intra-trimer overlap integrals ($p = 1.82 \times 10^{-2}$) and small inter-trimer overlap integrals ($q = 9.60 \times 10^{-4}$). In addition, the presence of large size trimers makes the $[Ni(9S3)_2]^{2+}$ molecules remain apart from each other. Using the empirical relations[34] between the bond length in a TCNQ molecule and its charge state, we estimate the valences of the TCNQ molecules are -0.69 for TCNQ (A) and -0.71 for TCNQ (B), respectively. It is considered that crystals **2** and **4**,

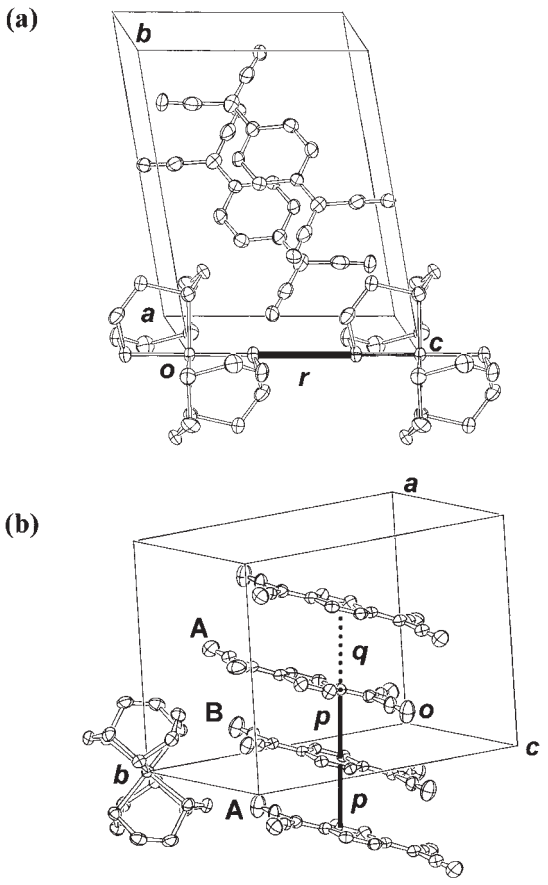

Fig. 1. The crystal structures of (a) $[Ni(9S3)_2](TCNQ)_2$ (**1**) and (b) $[Ni(9S3)_2](TCNQ)_3$ (**3**). Line $r = 3.838(6)$ Å represents the short S–S contact between $[Ni(9S3)_2]^{2+}$ cations, while lines *p* is the intra-trimer overlap integrals and *q* is the inter-trimer overlap integral between TCNQ molecules.

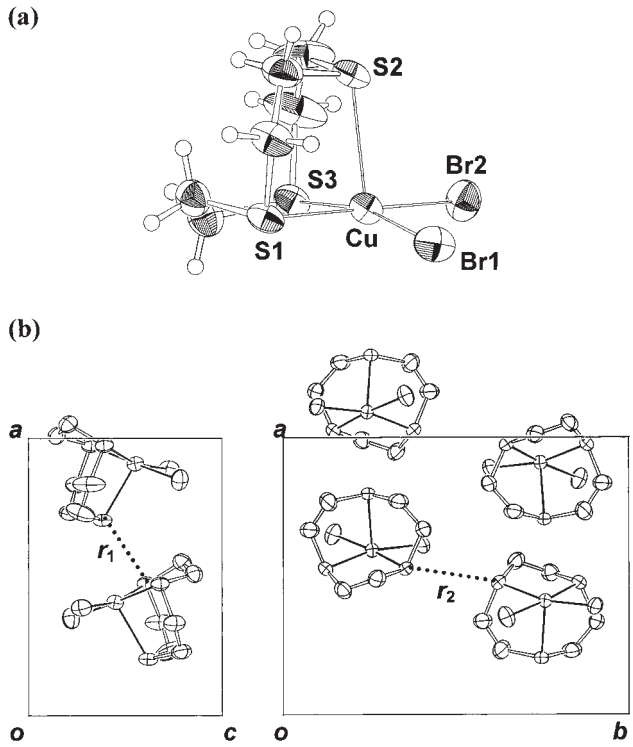

Fig. 2. (a) The molecular structure of a formula unit of $[Cu(9S3)Br_2]$ in **5**. There are two short Cu–S contacts, 2.288(15) and 2.321(14) Å for S1 and S3, respectively, and one long Cu–S contact, 2.614(13) Å for S2. The distances of Cu–Br are 2.406(9) and 2.447(9) Å for Br1 and Br2, respectively. (b) The crystal structure of **5**. $[Cu(9S3)Br_2]$ molecules form 1D chains spanned by intra-chain short S2–S3 contact r_1 ($= 3.543(4)$ Å) and elongated along the *a*-axis. The unit cell contains two chains connected by a weak inter-chain S1–S3 contact r_2 ($= 4.053(4)$ Å). The left panel shows a chain viewed parallel to the *b*-axis. The right panel is the unit cell containing two chains projected on the *ab*-plane.

isomorphous to **1** and **3**, respectively, have the same structural featured as those of **1** and **4**.

2.1.2 [Cu(9S3)Br$_2$] (5) and [Cu$_{1-x}$Ni$_x$(9S3)Br$_2$] ($x \sim 0.05$) (6): Figure 2 shows the crystal structure of **5**. The crystal consists of a five-coordinated complex of Cu, the same as [Pt(9S3)X$_2$] (X = Cl, Br, I) crystals.[35] The geometry of the molecule is described as an elongated square pyramid (Fig. 2a). Short inter-molecular S2–S3 contacts ($r_1 = 3.543(4)$ Å) connect [Cu(9S3)Br$_2$] molecules one-dimensionally along the *a*-axis, while the chains are coupled by very weak inter-chain S1–S3 contacts ($r_2 = 4.053(4)$ Å) along the *b*-axis.

When we substitute a small amount (~5%) of Cu ions with Ni ions, the crystal structure of [M(9S3)Br$_2$] is changed drastically, as exhibited in Fig. 3. The cause of the structural difference is not clearly understood. However, the slow crystal growth of **5** (4–5 weeks) and the fast crystal growth of **6** (1 day to 1 week) suggest that the arrangement of [Cu(9S3)Br$_2$] molecules is not well stabilized in **5**. The addition of a small amount of [Ni(9S3)Br$_2$], which has different intra-molecular metal–sulfur distances, results in an easy change in the molecular arrangement. This is supported by the fact that the [Ni(9S3)Br$_2$] concentration in **6** is independent of the initial concentration of NiBr$_2$ in the crystal growth. That is, there is a certain amount of [Ni(9S3)Br$_2$] suitable for the conversion of the crystal structures.

The intra-molecular and intra-chain structures are nearly the same between **5** and **6**, where the intra-chain S2–S3 contact ($r_1 = 3.495(4)$ Å) becomes shorter by only 1.4% in the latter to that of the former. On the contrary, the inter-chain coupling is more influenced by the substitution, where the arrangement of the chains changes with a 7.1% reduction of the inter-chain S1–S3 distance ($r_2 = 3.797(4)$ Å) to that of the latter. Therefore, it is expected that the substitution of Ni ions enhances the inter-chain magnetic interactions, as will be verified by the results of the magnetic susceptibilities.

2.1.3 [Ni(9S3)$_2$][Ni(bdt)$_2$]$_2$ (7) and [Co(9S3)$_2$][Ni(bdt)$_2$]$_2$ (8): Figures 4 and 5 show the crystal structures of **7** and **8**, which are isostructural to each other regardless of the cations. The unit cell consists of two crystallographically independent [Ni(bdt)$_2$]$^-$ anion molecules (A) and (B) which form a 2D cage-like structure on the plane spanned by the $a + c$ and $b + c$ directions, where a [M(9S3)$_2$]$^{2+}$ molecule is placed in the center of the cage, as shown in Fig. 4a. On the plane, there is a short S3–S5 contact between [M(9S3)$_2$]$^{2+}$ and [Ni(bdt)$_2$]$^-$ (A) with $r_1 = 3.772(2)$ and 3.806(2) Å for M = Ni and Co, respectively, and a CH–S6 contact between [Ni(bdt)$_2$]$^-$ (A) and [Ni(bdt)$_2$]$^-$ (B) molecules with $r_2 = 3.754(5)$ and 3.705(7) Å for M = Ni and Co, respectively. The 2D planes of the cage-like structure are stacked along the *c*-axis with the cage-like structure units shifted from each other by a half of the unit, as shown in Fig. 5. That is, a [Ni(bdt)$_2$]$^-$ (A) molecule of a plane lies on top of a [M(9S3)$_2$]$^{2+}$ molecule of the plane be-

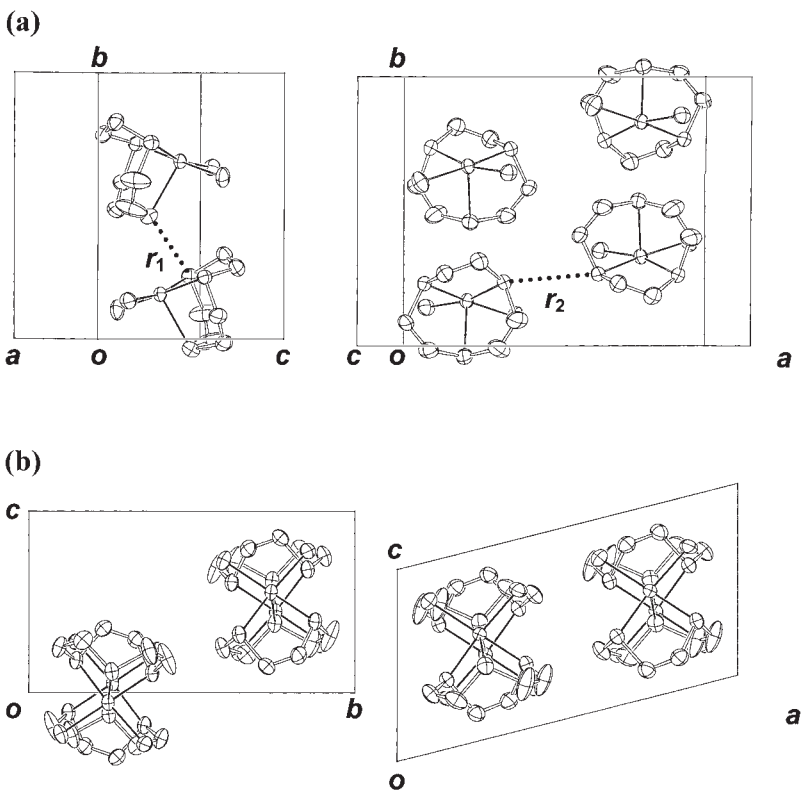

Fig. 3. (a) The crystal structure of [Cu$_{1-x}$Ni$_x$(9S3)Br$_2$] ($x \sim 0.05$) (**6**). A unit cell contains two chains of [Cu$_{1-x}$Ni$_x$(9S3)Br$_2$] molecules connected by intra-chain short S2–S3 contact r_1 (= 3.495(4) Å), which are loosely coupled by inter-chain short S1–S3 contact r_2 (= 3.797(4) Å). Intra-molecular short Cu–S contacts are 2.346(2) and 2.335(3) Å for S1 and S3, respectively, and one long Cu–S contact is 2.601(3) Å for S2. The distances of Cu–Br are 2.4193(19) and 2.4241(17) Å for Br1 and Br2, respectively. The labels of atoms are same as those shown in Fig. 2a. (b) The projections viewed along the 1D chains of [Cu(9S3)Br$_2$] (left) and [Cu$_{1-x}$Ni$_x$(9S3)Br$_2$] (right).

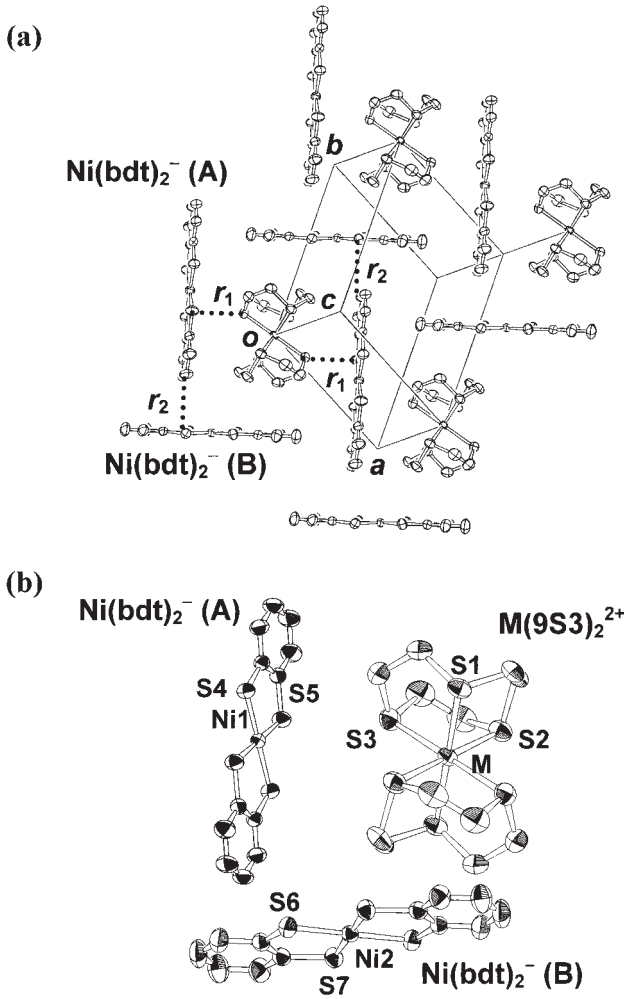

Fig. 4. The crystal structure of $[M(9S3)_2][Ni(bdt)_2]_2$ (M = Ni (**7**), Co (**8**)). (a) The plane of a cage-like structure on the plane spanned by the $a + c$ and $b + c$ directions. Four unit cells are shown in the figure. Dotted line r_1 represents the short S3–S5 contact between $[M(9S3)_2]^{2+}$ and $[Ni(bdt)_2]^-$ (A) molecules, while r_2 represents the CH–S6 contact between $[Ni(bdt)_2]^-$ (A) and $[Ni(bdt)_2]^-$ (B) anions; $r_1 = 3.772(2)$ and $r_2 = 3.754(5)$ Å for M = Ni, and $r_1 = 3.806(2)$ and $r_2 = 3.705(7)$ Å for M = Co. (b) Molecular structures of the constituent cation and anions.

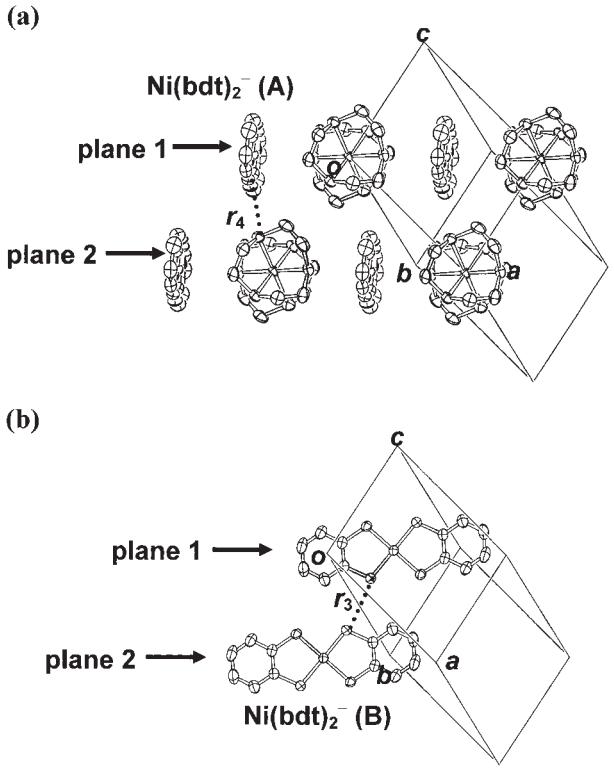

Fig. 5. The stacking of the planes along the c-axis direction in **7** and **8**. (a) $[M(9S3)_2]^{2+}$ and $[Ni(bdt)_2]^-$ (A) molecules and (b) $[Ni(bdt)_2]^-$ (B) molecules are shown. Dotted line r_3 represents the short S7–S7 contacts between $[Ni(bdt)_2]^-$ (B) anions, while r_4 represents the CH–S2 contacts between $[M(9S3)_2]^{2+}$ and $[Ni(bdt)_2]^-$ (A); $r_3 = 3.78$ and $r_4 = 3.98$ Å for M = Ni, $r_3 = 3.77$ and $r_4 = 3.93$ Å for M = Co.

neath (Fig. 5a), while a $[Ni(bdt)_2]^-$ (B) molecule of the upper plane lies on a $[Ni(bdt)_2]^-$ (B) of the lower plane with its center shifted parallel to the plane (Fig. 5b). Therefore, there are two kinds of inter-plane contacts generated. One is the contact between $[Ni(bdt)_2]^-$ (B) molecules with a short S7–S7 contact, $r_3 = 3.785(2)$ and 3.778(2) Å for M = Ni and Co, respectively, and the other is the CH–S2 contact between $[Ni(bdt)_2]^-$ (A) and $[M(9S3)_2]^{2+}$ with $r_4 = 3.920(6)$ and 3.937(6) Å for M = Ni and Co, respectively. Such structural features are the same between **7** and **8**, in spite of a difference in the coordination environments of $[M(9S3)_2]^{2+}$. In $[Ni(9S3)_2]^{2+}$, three crystallographically independent Ni–S coordination bonds have almost the same length (2.3967(11), 2.3849(10), and 2.3836(11) Å for S1, S2, and S3, respectively), whereas $[Co(9S3)_2]^{2+}$ has Jahn–Teller distortions in the Co–S distances; 2.4329(13), 2.285(1), and 2.2521(14) Å for S1, S2, and S3, respectively. The sulfur atoms of the latter two Co–S bonds, S2 and S3, are connected to the adjacent $[Ni(bdt)_2]^-$ through S3–S5 (r_1) and CH–S2 (r_4) contacts, while that of the former one, S1, does not participate in the inter-molecular contact.

2.2 Electrical Conductivity. Crystals **1**, **5**, **6**, **7**, and **8** are insulating ($\rho > 10^6$ Ω cm) at room temperature. TCNQ crystal **3** shows semiconductive behavior, with a resistivity of $\rho = 950$ Ω cm at room temperature and an activation energy of $E_a = 200$ meV. TCNQ molecules have a mixed valence of $-2/3$ in crystal **3**, but its small overlap integral between $TCNQ_3^{2-}$ trimers causes the high resistivity of **3**. Compared with highly conductive or metallic TCNQ mixed valence salts,[22–24] the molecular size of the cation is too large and the round shape of the cation is not fit for TCNQ to be stacked compactly to give a highly conductive column. This experimental finding is didactic from the point of achieving a highly conductive molecule-based magnet consisting of transition metal–crown thioether complexes. That is, the molecular sizes should be well balanced between the crown thioether complex and acceptor.

2.3 Magnetic Properties. 2.3.1 $[M(9S3)_2](TCNQ)_2$ (1, 2) and $[M(9S3)_2](TCNQ)_3$ (3, 4): The magnetic susceptibilities, χ, of **3** and **4** are characterized as paramagnetic with Curie constants $C = 0.971$ and 0.380 emu K mol^{-1} for **3** and **4**, respectively, and a Weiss temperature of $\Theta \sim 0$ K for both **3** and **4**.

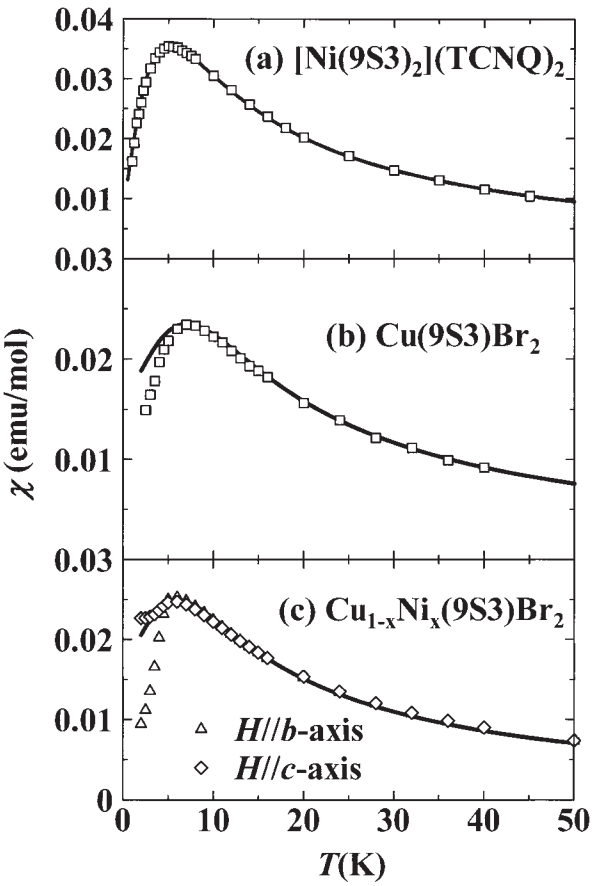

Fig. 6. The temperature dependence of magnetic susceptibilities of (a) $[Ni(9S3)_2](TCNQ)_2$ (**1**), (b) $[Cu(9S3)Br_2]$ (**5**), and (c) $[Cu_{1-x}Ni_x(9S3)Br_2]$ ($x \sim 0.05$) (**6**) measured in a magnetic field $H = 1$ T. No magnetic anisotropy is observed in **1** and **5**. Solid lines represent fitting curve calculated by the $S = 1$ 1D AF Heisenberg model (a) and $S = 1/2$ AF Heisenberg model (b, c).

The isolated structural features of $[Ni(9S3)_2]^{2+}$ molecules, which are well separated by $(TCNQ)_3^{2-}$ trimers, are responsible for the absence of magnetic interaction.

The temperature dependence of the susceptibility for **1** is shown in Fig. 6a. The susceptibility of **1** and **2** obeys the Curie–Weiss law, with antiferromagnetic (AF) Weiss temperatures $\Theta = -3.8$ K and -1.6 K and Curie constants $C = 0.967$ and 0.372 emu K mol^{-1} for **1** and **2**, respectively. The Curie constants correspond to one $S = 1$ spin of $[Ni(9S3)_2]^{2+}$ and $S = 1/2$ spin of $[Co(9S3)_2]^{2+}$, suggesting the singlet state of $TCNQ^-$ spins due to strong dimerization, as confirmed by the structural features. The susceptibility of **1**, which is isotropic over the whole measured temperature range, forms a broad hump around 10 K accompanied by a steep drop on the low temperature side of the hump. On the other hand, no anomaly in the susceptibility is observed in **2**, indicating the weakness of the interaction between $[Co(9S3)_2]^{2+}$ spins having $S = 1/2$ instead of $S = 1$ for $[Ni(9S3)_2]^{2+}$.

Comparing the inter molecular distances of **1** with those of **3**, it is observed that **1** has a shorter S–S atomic contact length (3.838(6) Å) and longer Ni^{2+}–Ni^{2+} distance (8.627(9) Å) than those of **3** (4.685(3) and 7.761(3) Å), while the intra molecular Ni^{2+}–S distances have roughly same value (2.383(4), 2.400(4), and 2.403(4) Å for **1** and 2.371(1), 2.389(1), and 2.390(1) Å for **3**, respectively). The difference in the inter molecular distances between **1** and **3**, and the similarity of the intra molecular distances indicate that the strength of the magnetic interaction mainly depends on the inter molecular S–S contact in transition metal complexes of crown thioethers, taking into account the difference in the strength of exchange interactions.

The susceptibility of **1** is well described by the uniform AF Heisenberg chain model[36] with $S = 1$ given by following equation,

$$\chi = (2N_A g^2 {\mu_B}^2/3|2J|)\cdot\{(X^2 + 0.5X + 0.1) /(X^3 + 1.885382X^2 + 1.812404X + 1.607565)\}, \quad (1)$$

where

$$X = \frac{k_B T}{|2J|}, \quad (2)$$

N_A, g, μ_B, and k_B are Avogadro's number, a g-value assumed as $g \sim 2$ for Ni^{2+}, the Bohr magneton and Boltzmann's constant. The exchange interaction J is defined in the following Hamiltonian:

$$H = -2J \sum_i \boldsymbol{S}_i \boldsymbol{S}_{i+1}. \quad (3)$$

The absence of 3D ordering proves the negligible contribution of inter-chain interactions, which is reasonably understood from the absence of close inter-chain molecular contact in the structural consideration (see Fig. 1a). The intra-chain magnetic interaction J is estimated from the fitting at $J = -3.9$ K, which is stronger than expected based on the fact that the S–S distance between $[Ni(9S3)_2]^{2+}$ molecules (= 3.838(6) Å) is considerably larger than the corresponding van der Waals distance (= 3.7 Å). This apparent inconsistency verifies that a large spin density exists at the surrounding sulfur atoms in the ligand of $[Ni(9S3)_2]^{2+}$, which is expected from the strong π-acidity of crown thioethers.[18,19] Therefore, the experimental finding of **1** proves the importance of crown thioether complexes of transition metals as a building block in designing molecule-based magnets with hybrid structures.

The susceptibility of **2** is described by the Bonner–Fisher model of a 1D AF chain[37,38] with $S = 1/2$

$$\chi = (N_A g^2 {\mu_B}^2/k_B T)\cdot\{(0.25 + 0.14995X + 0.30094X^2) /(1.0 + 1.9862X + 0.68854X^2 + 6.0626X^3)\}, \quad (4)$$

where

$$X = \frac{|J|}{k_B T}, \quad (5)$$

and we assume $g \sim 2$. The intra-chain interaction is estimated to be $J = -1.3$ K, which is considerably smaller than that of isostructural **1** having the $[Ni(9S3)_2]^{2+}$ cation. The believed origin of the decrease of the intra-chain interaction is the Jahn–Teller distortion of $[Co(9S3)_2]^{2+}$, as we will discuss in the magnetic susceptibility of $[M(9S3)_2][Ni(bdt)_2]_2$.

2.3.2 $[Cu(9S3)Br_2]$ (5) and $[Cu_{1-x}Ni_x(9S3)Br_2]$ ($x \sim 0.05$) (6): The susceptibilities of **5** and **6** are shown in Fig. 6b and 6c. χ obeys the Curie–Weiss law, where the Curie constants and the AF Weiss temperatures are estimated as $C = 0.381$

emu K mol^{-1} and $\Theta = -4.2$ K for **5** and $C = 0.395$ emu K mol^{-1} and $\Theta = -3.6$ K for **6**. These values of the Curie constants correspond to one Cu^{2+} $S = 1/2$ spin per formula unit, in addition to a small contribution from Ni^{2+} $S = 1$ in the case of **6**. χ takes a broad hump around 7 and 6 K for **5** and **6**, respectively. A fitting is made with the Bonner–Fisher model where we assume $g \sim 2$ for both Cu^{2+} and a small amount of Ni^{2+} ions in **5** and **6**, and where intra-chain interactions J are estimated as $J = -5.4$ K and -4.7 K for **5** and **6**, respectively. The nearly equal values of the intra-chain interaction in **5** and **6** are considered to be due to the same intra-chain structure of the crystals. The behavior of χ on the low temperature side of the hump is different between **5** and **6**. In the crystal **5**, χ shows a reduction from that expected with the 1D antiferromagnetic Heisenberg model with weak inter-chain interactions, in addition to the absence of anisotropic behavior. In contrast, for **6**, an anisotropy appears between the field directions parallel to the *b*- and *c*-axes, suggesting an onset of an AF transition at $T_N = 5$ K, where the spin easy axis is oriented parallel to the *b*-axis in the ordered state. The difference is associated with the 2D nature of **6**, which is generated by the modification of the arrangement of the $[M(9S3)Br_2]$ chains by the substitution, as can be seen in the considerable reduction of the S1–S3 contact.

2.3.3 $[Ni(9S3)_2][Ni(bdt)_2]_2$ (7) and $[Co(9S3)_2][Ni(bdt)_2]_2$ (8): The temperature dependence of the magnetic susceptibility has previously been reported in Ref. 29 for **7** under the fields applied in three directions *x*, *y*, and *z* (see Figs. 7b and 7c for the definition of *x*, *y*, and *z*). The susceptibility of **7** obeys the Curie–Weiss law at high temperatures above ca. 150 K with a negative Weiss temperature of $\Theta = -6.5$ K and Curie constant $C = 1.76$ emu K mol^{-1}, the latter of which corresponds to one $S = 1$ spin of $[Ni(9S3)_2]^{2+}$ and two $S = 1/2$ spins of $[Ni(bdt)_2]^-$ per formula unit. Below ca. 8 K, anisotropic behavior emerges between the different field directions, where the susceptibility makes sharp peaks at 5.8 and 6.2 K in the *x*- and *z*-directions, respectively. In addition, a susceptibility minimum is found at 4.1 K in the *z*-direction, below which the χ increases as the temperature is lowered. In contrast, only a broad hump is produced at 5.2 K in the *y*-direction, on the low temperature side of which χ shows a weak decrease. The slight increase of χ below 4.1 K in $H \parallel z$ and the non zero value of χ in $H \parallel x$ extrapolated to 0 K may be due to a small misalignment of the crystal and/or the fact that the weak-ferromagnetic axis deviates slightly from the *y*-direction. The AC susceptibility at 10 Hz shows a sharp peak at 6.2 K. These experimental findings, in addition to the presence of a remanent magnetization which will be discussed in the results of magnetization curves, suggest an onset of a weak-ferromagnetic (WF) transition with a Néel temperature $T_N = 6.2$ K, where the *x*- and *y*-directions correspond to the spin easy axis and WF axis, respectively.

Figure 7a shows the magnetization curves at $T = 2$ K. Below T_N, the magnetization curve of $H \parallel y$ shows a hysteresis loop with a discontinuous change at a coercive force $H_C = 20$ mT and remanent magnetization $M_{REM} = 0.18$ μ_B, as shown in the inset of Fig. 7a. The existence of M_{REM} provides evidence of weak-ferromagnetism, though the value is quite large compared to that for ordinary weak-ferromagnets. A spin flop is observed at about $H_{SF} = 1.7$ T in $H \parallel x$, as proved by the S-shaped magnetization curve, which is consistent with the fact that χ steeply approaches zero as the temperature goes to 0 K only in this direction. These suggest that the easy axis is oriented in the *x* direction. It should be noted that χ increases even for the easy axis in the temperature range $5.8 < T < 6.2$ K ($= T_N$) in a similar fashion as that along the WF axis. This behavior can be understood as the consequence of the XY character of the spin system. This interpretation is confirmed by the M_{REM} measurement shown in Fig. 7d. Judging from the existence of the remanent magnetization in the *x*- and *y*-directions and its absence in the *z*-direction, the moment of weak-ferromagnetism is considered to lie on the *x*–*y* plane below T_N. M_{REM} rapidly increases in $H \parallel x$ in the vicinity of T_N as the temperature decreases, followed by the increase in $H \parallel y$. Below that temperature range, the remanent magnetization for $H \parallel x$ decreases after a broad hump around 5.7 K, whereas that for $H \parallel y$ continuously increases and plateaus below ca. 5 K. The overwhelming behavior of the remanent magnetization for $H \parallel y$ below 5.7 K proves a rotation of the moment of the weak-ferromagnetism from the *x*-direction to the *y*-direction at ca. 5.7 K. Considering the thin planar crystal shape, as mentioned in the experimental section, the *x*- and *y*-directions correspond to the thickness and length dimensions of the thin planar crystal, respectively, as shown in Fig. 7c. The rotation of the WF axis is, therefore, considered to be partly caused by the demagnetization field, which becomes large when the applied field is directed normal to the plane. The demagnetization field, which is generated by the remanent magnetization (0.1 μ_B at 5.7 K in large crystal) for $H \parallel x$, is estimated to be about 1 mT if we assume that the plate is infinite. In contrast, only a negligible demagnetization field is generated when the field is applied along the *y*-axis. Therefore, the small anisotropy of ca. 1 mT works when the WF direction is rotated between the *x*- and *y*-axes, as an external perturbation inherited by the crystal shape. This is verified by the change of the rotation, as shown in Fig. 7e, when we cut the crystal so as to make the lengths be roughly the same in the *x*- and *y*-directions. In the cut sample, the rotation temperature changes from 5.7 K to 4.9 K owing to the reduction of the demagnetization field.

The XY character of **7** is also supported by the crystal structure as follows. $[Ni(9S3)_2]^{2+}$ has the very isotropic octahedral coordination, which provides isotropic magnetic properties, as confirmed by the isotropic susceptibility of crystal **1**, to which only $[Ni(9S3)_2]^{2+}$ contributes. On the other hand, the crystal field axes of $[Ni(bdt)_2]^-$ anions (A) and (B) are orthogonal to each other, where molecular planes lie perpendicular to the *x*- and *y*-directions, respectively. Therefore, the anisotropy of $[Ni(bdt)_2]^-$ molecules does not play a serious role in determining the direction of the weak-ferromagnetic moment in the *xy* plane. As a result, the WF axis of the thin planar crystal of **7** is easily rotated to the *y*-direction by the demagnetization field in the temperature range $4.9 \text{ K} < T < 6.2$ K. However, the WF axis is also rotated below 4.9 K even in the cut sample, where the demagnetization effect is partially present. This fact suggests that there is a small magnetic anisotropy in the *xy*-plane which governs the WF axis in the low temperature region, though the origin of the anisotropy remains unclear. The anisotropy also causes the enhancement of the spin flop field, the val-

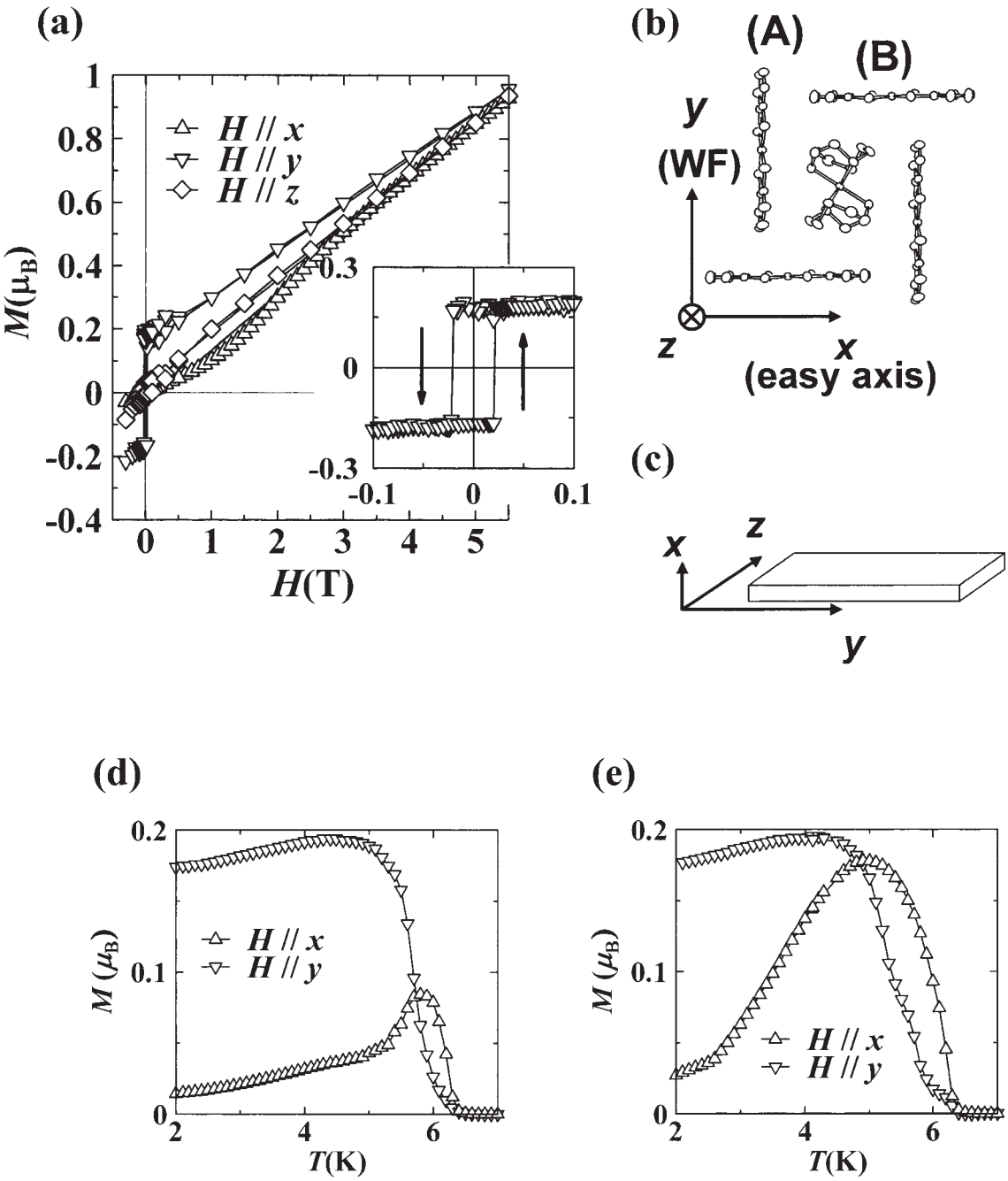

Fig. 7. (a) The magnetization curves of $[Ni(9S3)_2][Ni(bdt)_2]_2$ (**7**) at 2 K in the field applied in the three directions. The inset is the enlargement of the low magnetic field region for $H \parallel y$. (b) The definition of directions x, y, and z. (A) and (B) represent $[Ni(bdt)_2]^-$ (A) and $[Ni(bdt)_2]^-$ (B) molecule, respectively. (c) The relation between the directions and the crystal shape. (d) Temperature dependence of remanent magnetization with a weak external magnetic field $H = 0.3$ mT applied parallel to the x and y directions during heating processes. (e) Remanent magnetization with $H = 0.3$ mT for fractional crystals obtained by cutting the sample of **7**. The crystal lengths of each individual crystal are roughly same in the x- and y-directions.

ue of which ($H_{SF} = 1.7$ T) is much larger than that expected from the anisotropy caused by the demagnetization field.

Figure 8a shows the temperature dependence of the susceptibility of **8**. χ obeys the Curie–Weiss law at high temperatures above ca. 100 K with negative Weiss temperature $\Theta = -2.3$ K and Curie constant $C = 1.17$ emu K mol^{-1}, the latter of which corresponds to one $S = 1/2$ spin of $[Co(9S3)_2]^{2+}$ and two $S = 1/2$ spins of $[Ni(bdt)_2]^-$ per formula unit. Below 4 K, anisotropy emerges between the three field directions, where χ forms a peak at 2.6 K for $H \parallel z$. The AC susceptibility at 10 Hz also forms a peak at this temperature, suggesting the onset of an AF transition at $T_N = 2.6$ K. For the $H \parallel x$ and y directions, χ increases even below T_N, which is the consequence of the weak-ferromagnetism. The behaviors of the magnetization curves of the three directions at $T = 2$ K shown in Fig. 8b are very similar to each other except the hysteresis loop in

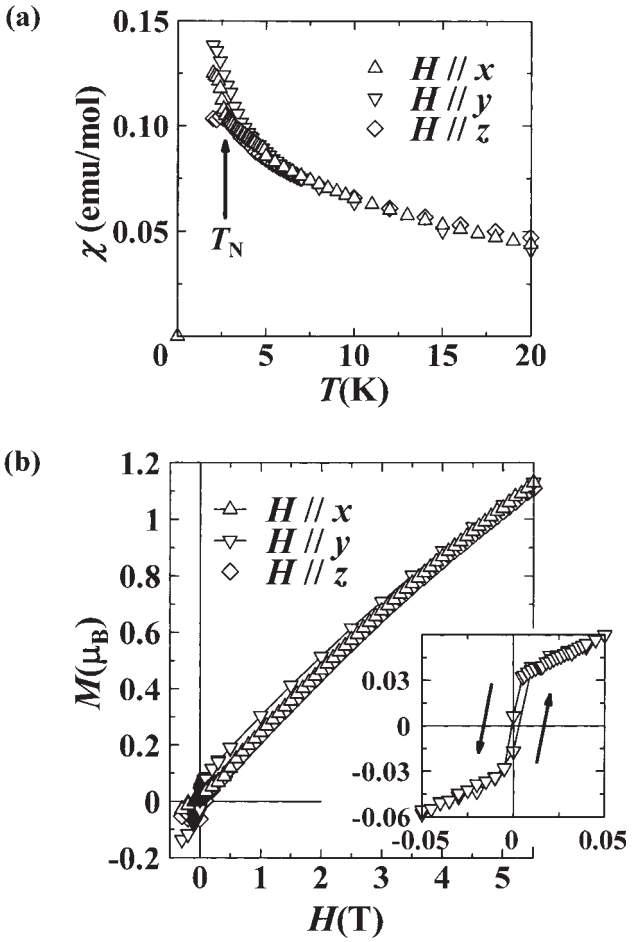

Fig. 8. (a) The temperature dependence of the susceptibilities of $[Co(9S3)_2][Ni(bdt)_2]_2$ (**8**) measured with a magnetic field $H = 0.1$ T applied parallel to the *x*-, *y*- and *z*-directions (see Fig. 7b for the definitions of *x*, *y*, and *z*). The weak-ferromagnetic transition temperature $T_N = 2.6$ K is determined from the AC susceptibility measurement. (b) The magnetization curves of $[Co(9S3)_2][Ni(bdt)_2]_2$ at 2 K. Inset is the enlargement of the low magnetic field region of $H \parallel y$.

$H \parallel y$. In $H \parallel y$, the magnetization shows a hysteresis loop with a coercive force $H_C = 1$ mT and remanent magnetization $M_{REM} = 0.015\ \mu_B$, as shown in the inset of Fig. 8b. These values are about one-twentieth smaller than those of **7**. The WF axis is confirmed to be aligned parallel to the *y*-direction because a hysteresis loop is observed only when the magnetic field is applied parallel to this direction. However, the increase of χ below T_N not only for $H \parallel y$ but also for $H \parallel x$ suggests that the weak-ferromagnetic moment of **8** is also rotated in the *xy* plane when we use a thin planar crystal, as in **7**. In connection to this, the small value of M_{REM} considerably diminishes the demagnetization field effect (~0.1 mT), which makes the rotation easier. As a result of this easiness in the rotation, a spin flop transition is not observed clearly because the spin is easily rotated in a very weak magnetic field.

2.4 The Origin of the Weak-Ferromagnetism of $[M(9S3)_2][Ni(bdt)_2]_2$ ((7) and (8)). Here, the origin of weak-ferromagnetism in **7** and **8** is discussed as a main issue, since weak-ferromagnetism is unconventional in molecule-based magnets that have been investigated. For searching for the origin of weak-ferromagnetism, information about the magnetic structure is necessary. As will be discussed later, the magnetic structure consists of alternate chains of $[M(9S3)_2]^{2+}$ and $[Ni(bdt)_2]^-$ (A) molecules and AF chains of $[Ni(bdt)_2]^-$ (B) molecules. There are two typical candidates for the origin: Dzyaloshinskii–Moriya (DM) interactions and the coexistence of different magnetic sites having different anisotropy axes.[39–42] However, among these, the DM interaction seems to not be suitable for the origin in the present case because of the extraordinary large remanent magnetization of **7**, which corresponds to ca. 7° of the canting angle of a ferrimagnetic (FI) chains of $[Ni(9S3)_2]^{2+}$ and $[Ni(bdt)_2]^-$ (A) molecules, while the AF chains of $[Ni(bdt)_2]^-$ (B) molecules cannot take DM interactions because of the presence of an inversion center. In addition, the difference in the anisotropy axes of cations and/or anions is also ruled out, as will be seen in the later discussion.

For discussing weak-ferromagnetism, we first take crystal **7**, which has the extraordinary large remanent magnetization. According to the crystal structure of **7**, there are four magnetic interactions J_1, J_2, J_3, and J_4 associated with inter-molecular atomic contacts r_1, r_2, r_3, and r_4 , respectively (see Figs. 4 and 5). Judging from the local spin density, which has large values at the central metal atom and adjacent sulfur atom of the ligand,[18,19,43] J_1 and J_3 through short S–S contacts are considered to be strong, while J_2 and J_4 through CH–S contacts are weak. Comparing J_2 with J_4, J_2 is stronger than J_4 because r_4 is ca. 5% longer than r_2. In short, $|J_1|, |J_3| \gg |J_2| > |J_4|$. Therefore, two kinds of chains spanned by J_1 and J_3 work as fundamental structural units in explaining the magnetic structure. One is the alternate FI chains (#1 chains) elongated parallel to the $(a + c)$ direction, which consist of $[Ni(9S3)_2]^{2+}$ molecules and $[Ni(bdt)_2]^-$ (A) molecules bonded by J_1, and the other is uniform AF chains (#2 chains) elongated parallel to the *c*-axis, which consist of $[Ni(bdt)_2]^-$ (B) molecules bonded by J_3. The magnetic structure model is schematically shown in Fig. 9. The absence of the spontaneous magnetization associated with the FI structure of #1 chains below T_N indicates an antiparallel arrangement of magnetic moments between FI chains. The magnetic anisotropies of $[Ni(9S3)_2]^{2+}$ and $[Ni(bdt)_2]^-$ (A) are, if they exist, compensated between two #1 chains aligned in antiparallel, resulting in the absence of a spontaneous magnetization. Similarly, the anisotropies of $[Ni(bdt)_2]^-$ (B) molecules in #2 chains are also compensated between adjacent $[Ni(bdt)_2]^-$ (B) molecules in a #2 chain. As a result, magnetic anisotropies of cations and anions are also excluded a candidates of the origin of the weak-ferromagnetism.

In contrast, a competition of two AF interactions, J_2 and J_4, can be a candidate for the origin of the weak-ferromagnetism. In the first step of the discussion, we take only J_1, J_2, and J_3 to consider a possible spin structure, as shown in Fig. 10a. In this structure, the spin of a $[Ni(bdt)_2]^-$ (A) in #1 chain, which is strongly coupled by J_1 with the spins of $[M(9S3)_2]^{2+}$ in the same chain, is connected antiferromagnetically to an AF #2 chain by J_2. In the next step, J_4, the weakest inter-chain interaction between #1 chains, is introduced to the magnetic structure model (Fig. 10b). The spin configuration of Fig. 10b is frustrated because of the parallel spin configuration against

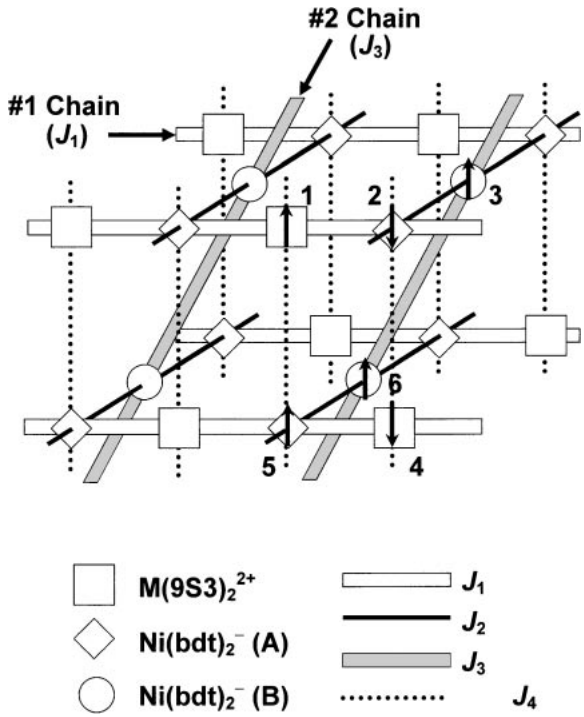

Fig. 9. The schematic of the magnetic structure in $[M(9S3)_2][Ni(bdt)_2]_2$, which consists of alternate $[M(9S3)_2]^{2+}$–$[Ni(bdt)_2]^-$ chains (#1 chain) and uniform $[Ni(bdt)_2]^-$ chains (#2 chain). Six arrows numbered with 1 to 6 represent the spins in six sublattices; two $[M(9S3)_2]^{2+}$ (1, 4), two $[Ni(bdt)_2]^-$ (A) (2, 5), and two $[Ni(bdt)_2]^-$ (B) (3, 6).

AF interaction J_4 between the two FI #1 chains. To reduce the energy caused by the spin conflict, the easy axes of the spins in the #1 chains are forced to be canted (Fig. 10c). In this scenario, the collinear structure in the #1 chain is assumed to be conserved against the inter-chain interactions because of strong intra-chain AF interaction J_1. This means that the spins of FI chains are canted in the same direction in concert with respect to the spins of the adjacent FI chain, giving rise to the generation of a spontaneous magnetic moment. The relaxation of the constraint on the collinear structure will give a slight modification without any loss of validity. In this model, magnetic anisotropies and anisotropic interactions are not necessary, and the extraordinary large remanent magnetization is the natural consequence, as follows. The canting angle of the FI chains rapidly increases when the ratio of J_4/J_2 increases, where the canting of the FI structure is accompanied by a large remanent magnetization. Therefore, this model is suitable to explain the origin of the weak-ferromagnetism of **7**.

In the cobalt(II) complex salt **8**, the spin canting of the #1 chains may also occur, but such a canting cannot cause a spontaneous magnetization because #1 chains have no net magnetic moment. A possible case of weak-ferromagnetism in **8** is the spin canting of $[Ni(bdt)_2]^-$ (B) in #2 chains (θ_3 and θ_6) and/or the difference of the canting angles between $[Co(9S3)_2]^{2+}$ and $[Ni(bdt)_2]^-$ (A) ($\theta_1 - \theta_2$ and $\theta_4 - \theta_5$) in #1 chains. Though J_3 is stronger than J_2 and J_4, the spin canting of #1 chains, if it exists, can induce a small spin canting in #2 chains. Such a

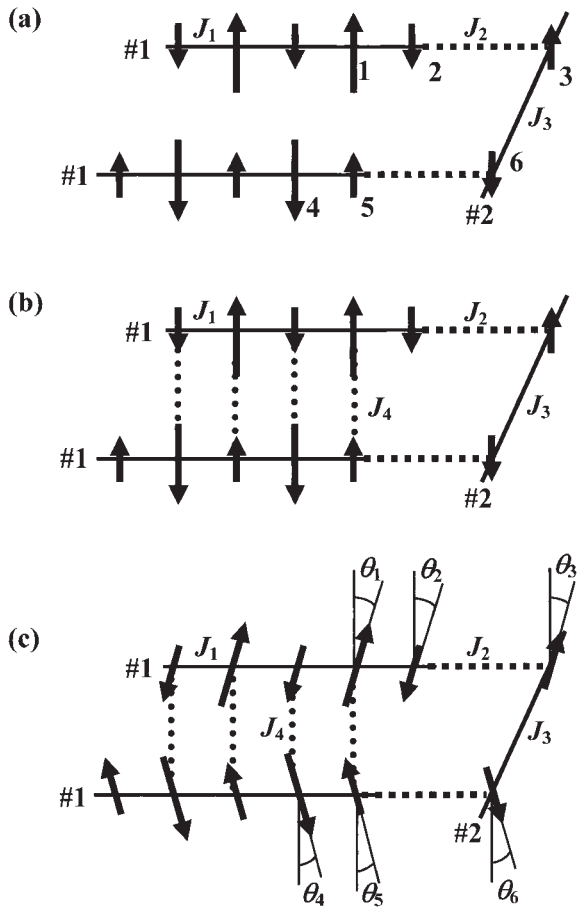

Fig. 10. (a) The magnetic structure model of $[Ni(9S3)_2]$-$[Ni(bdt)_2]_2$ with three AF exchange interactions J_1, J_2, and J_3 ($|J_1|$, $|J_3| \gg |J_2|$). Only three chains (two #1 chains and a #2 chain) are shown for clarity. Numbered arrows represent the six sublattices corresponding to those of Fig. 9. (b) Introducing the weakest AF inter-chain interaction J_4 destabilizes the spin configuration of (a). (c) Magnetic structure model with J_1, J_2, J_3, and J_4, where spin frustration effect is reduced by canting the spins of #1 and #2 chains. Angle θ_i represents the canting angle of ith sublattice.

canting also contributes to the weak-ferromagnetism in both **7** and **8**, however, strong J_1 and J_3 allows only a very small intra-chain canting angle. Furthermore, the weakening of the inter-chain interaction $-2J_4\boldsymbol{S}_1 \cdot \boldsymbol{S}_5$ between #1 chains caused by employing $[Co(9S3)_2]^{2+}$ ($S = 1/2$) in place of $[Ni(9S3)_2]^{2+}$ ($S = 1$) tends to diminish the competition between J_2 and J_4, resulting in the reduction of canting angles. Consequently, only weak weak-ferromagnetism is observed. The reduced remanent magnetization in **8** brings about the decrease of the demagnetization field, resulting in the reduction of the anisotropy energy. Such a small anisotropy energy is the reason for the small coercive force in **8**. Similar canting of #2 chains induced by #1 chains also can occur in the nickel(II) complex salt **7**, but such a contribution of the canting to the weak-ferromagnetism is not so large in **7** because the weak-ferromagnetism of **7** having an FI structure is mainly governed by the canting between #1 chains.

Finally, we discuss the magnetic structure on the basis of the mean field approximation. Before calculation, we empirically estimate the values of J_1 and J_3. In the high temperature region, χ is considered to be described as the simple sum of the contributions from a FI #1 chains and an AF #2 chains for **7** or the sum of an AF #1 chains and an AF #2 chains for **8** because inter-chain interactions are orders of magnitude weaker than intra-chain interactions, where the strength of the inter-chain interactions is considerably small in comparison with the thermal energy. From the fitting of χ by the FI chain model[44] of $S = 1$ and 1/2,

$$\chi = (N_A{\mu_B}^2 g^2/k_B T)\cdot\{(-0.034146801X^3 + 2.8169306411X^2 - 7.2310013697X + 11)/(1.29663274X^2 + 0.69719013595X + 12)\}, \quad (6)$$

where

$$X = \frac{|2J|}{k_B T}, \quad (7)$$

and the AF chain model (Eq. 4)[33,34] in the region of 100 K $< T <$ 300 K, we obtained $J_1 = -12.6$ K and $J_3 = -4.9$ K for **7** and $J_1 = -4.1$ K and $J_3 = -4.5$ K for **8**. The large difference in J_1 between **7** and **8** is explained by the Jahn–Teller distortion of **8**. In the $[Co(9S3)_2]^{2+}$ salt **8** having the electron configuration[45] of an octahedral Co^{2+} ion $(t_{2g})^6(e_g)^1$, only one electron in the e_g state, which can contribute to the magnetism, tends to occupy the d_{z^2} orbital directed to the S1 atom, which has no inter-molecular contact. On the other hand, in the electron configuration of an octahedral Ni^{2+} ion $(t_{2g})^6(e_g)^2$, magnetic electrons occupy not only the d_{z^2} orbital directed at the S1 atom, but also the $d_{x^2-y^2}$ orbital directed at S2 and S3 atoms which have inter-molecular contacts. As a result, the inter-molecular interaction of $[Co(9S3)_2]^{2+}$ becomes weaker than that of $[Ni(9S3)_2]^{2+}$.

Using these J_1 and J_3 values, M_{REM} of **7** and **8** at 2 K was calculated for various values of J_2 and J_3 on the basis of the six-sublattices model (two-sublattices of each of $[Ni(9S3)_2]^{2+}$, $[Ni(bdt)_2]^-$ (A) and $[Ni(bdt)_2]^-$ (B), see Fig. 9) in the mean field approximation. In the calculation, we assume that the spins can be rotated only in the *xy* plane with no in-plane anisotropy for simplicity, which is not contrary to the nature of **7** and **8**. The mean field $\boldsymbol{H}_i$ and effective magnetic moment $\boldsymbol{M}_i$ of sublattice *i* (see Fig. 9 for the definitions of *i*) are represented as follows;

$$\left.\begin{aligned}
\boldsymbol{H}_1 &= 2A_1\boldsymbol{M}_2 + 2A_4\boldsymbol{M}_5,\\
\boldsymbol{H}_2 &= 2A_1\boldsymbol{M}_1 + 2A_2\boldsymbol{M}_3 + 2A_4\boldsymbol{M}_4,\\
\boldsymbol{H}_3 &= 2A_2\boldsymbol{M}_2 + 2A_3\boldsymbol{M}_6,\\
\boldsymbol{H}_4 &= 2A_1\boldsymbol{M}_5 + 2A_4\boldsymbol{M}_2,\\
\boldsymbol{H}_5 &= 2A_1\boldsymbol{M}_4 + 2A_2\boldsymbol{M}_6 + 2A_4\boldsymbol{M}_1,\\
\boldsymbol{H}_6 &= 2A_2\boldsymbol{M}_5 + 2A_3\boldsymbol{M}_3,
\end{aligned}\right\} \quad (8)$$

$$\boldsymbol{M}_i = N_A g\mu_B S_i \frac{\boldsymbol{H}_i}{|\boldsymbol{H}_i|} B_S\left(\frac{S_i g\mu_B \boldsymbol{H}_i}{k_B T}\right), \quad (9)$$

where $B_S(x)$ and S_i are the Brillouin function and the spin of sublattice *i* ($S_i = 1$ for $i = 1$ and 4, 1/2 for $i = 2$, 3, 5, and 6 in **7**; $S_i = 1/2$ for $i = 1$ to 6 in **8**), respectively, and

$$A_i = \frac{J_i}{N_A g^2 {\mu_B}^2}. \quad (10)$$

We assume $g \sim 2$ for all the spins irrespective of the magnetic ions. The calculation was carried out until $\boldsymbol{M}_i$, the initial value of which were randomly selected, become self-consistently determined. If the calculated values of $\boldsymbol{M}_i$ depend on the set of initial values because of existence of the local minima, we select the state which has the lowest energy *E* defined as follows after several trials,

$$\begin{aligned} E &= \sum_{i,j} -2J_{ij}\boldsymbol{M}_i\boldsymbol{M}_j \\ &= -2\cdot 2J_1(\boldsymbol{M}_1\boldsymbol{M}_2 + \boldsymbol{M}_4\boldsymbol{M}_5) - 2\cdot 2J_2(\boldsymbol{M}_2\boldsymbol{M}_3 + \boldsymbol{M}_5\boldsymbol{M}_6) \\ &\quad - 2\cdot 2J_3\boldsymbol{M}_3\boldsymbol{M}_6 - 2\cdot 2J_4(\boldsymbol{M}_1\boldsymbol{M}_5 + \boldsymbol{M}_2\boldsymbol{M}_4). \end{aligned} \quad (11)$$

Figures 11a and 11b show the calculated M_{REM} at 2 K of **7** and **8**, respectively, which has a non-zero value. Furthermore, the weak-ferromagnetic region (WFM) exists not only in $[Ni(9S3)_2][Ni(bdt)_2]_2$, but also in $[Co(9S3)_2][Ni(bdt)_2]_2$. The small value of WFM in $[Co(9S3)_2]^{2+}$ and large value of WFM in $[Ni(9S3)_2]^{2+}$ are in good agreement with the values experimentally obtained. In the WFM region, the calculated spin arrangement can accurately reproduce that shown in Fig. 10c. For example, at $(J_2, J_4) = (-0.50$ K, -0.064 K) in **7** with $M_{REM} = 0.18\ \mu_B$, the calculated canting angles, θ_i, defined in Fig. 10c are 10.0° for $i = 1$, 2, 4, and 5, 0.25° for $i = 3$ and 6, while the sublattice magnetic moments $|\boldsymbol{M}_i|$ calculated are approximately the same as the values of S_i due to the reduced thermal agitation at the low temperatures. The small values of $(\theta_1 - \theta_2)$, $(\theta_4 - \theta_5)$, θ_3 and θ_6 suggest that strong intra-chain interactions stabilize the FI structure of #1 chains and the AF structure of #2 chains in the WFM region, while weak-ferromagnetism is mainly caused by the canting of the FI chains. In contrast, the calculated M_{REM} of **8** is associated with both the canting of #2 chains (θ_3 and θ_6) and difference between canting angles ($\theta_1 - \theta_2$ and $\theta_4 - \theta_5$), as expected from the model mentioned above. For example, at $(J_2, J_4) = (-0.22$ K, -0.066 K) in **8** with $M_{REM} = 0.015\ \mu_B$, the canting angles defined in Fig. 10c are calculated as 35.1° for $i = 1$ and 4, 34.6° for $i = 2$ and 5, and 0.40° for $i = 3$ and 6. It should be noted that a quantitative discrepancy in the absolute value of M_{REM} is present between the calculated and the measured value. Indeed, in the calculation, the region of $M_{REM} \sim 0.18\ \mu_B$, which is the value observed in the actual crystal, is very small and M_{REM} rapidly increases to over 0.6 μ_B when $|J_4|$ increases. This discrepancy may come from the simplification of the mean field approximation.

3. Conclusion

The structures and magnetic properties were investigated for a new class of molecule-based magnets based on transition metal complexes with crown thioethers as a key building block. The TCNQ salt $[Ni(9S3)_2](TCNQ)_2$ consists of a 1D $[Ni(9S3)_2]^{2+}$ chain and well-separated $(TCNQ)_2{}^{2-}$ dimer. The magnetic properties of 1D $[Ni(9S3)_2]^{2+}$ chain and $(TCNQ)_2{}^{2-}$ dimer are characterized as 1D antiferromagnet with strong AF inter-molecular interactions ($J = -3.8$ K) and a non-magnetic dimmer. $[Co(9S3)_2](TCNQ)_2$ has weak antifer-

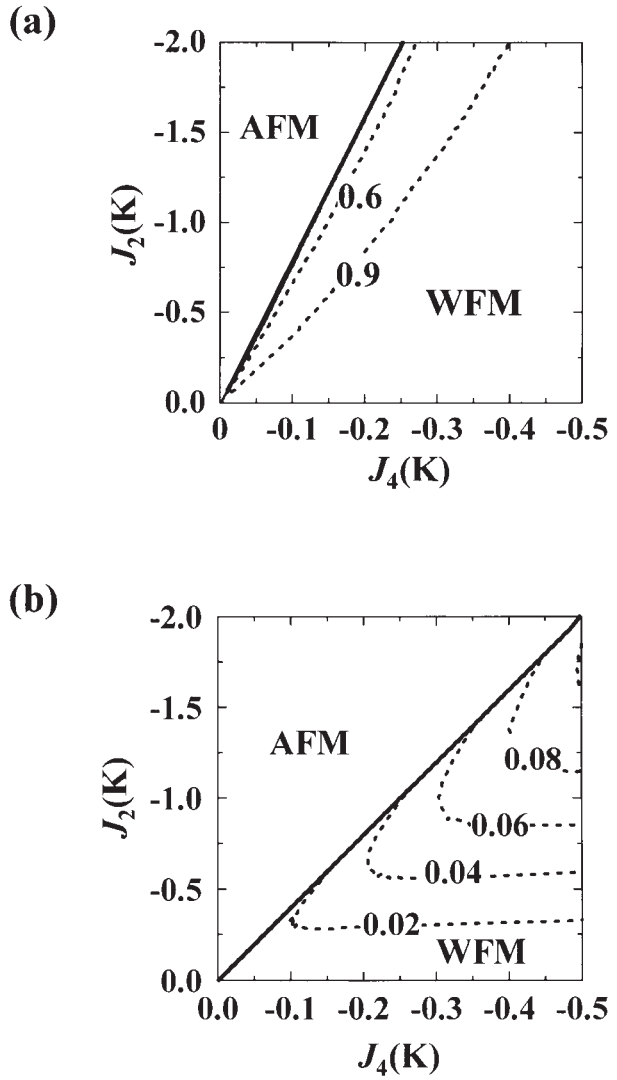

Fig. 11. The remanent magnetization (M_{REM}) and phase diagram calculated by mean field approximation at 2 K as functions of J_2 and J_4 for (a) $[Ni(9S3)_2][Ni(bdt)_2]_2$ and (b) $[Co(9S3)_2][Ni(bdt)_2]_2$. The solid lines represent the boundary between weak-ferromagnetic state (WFM) and antiferromagnetic state (AFM). The dotted lines represent $M_{REM} = 0.3$ (near the boundary of WFM/AFM), 0.6 and 0.9 μ_B for $[Ni(9S3)_2][Ni(bdt)_2]_2$ and 0.02, 0.04, 0.06, 0.08, and 0.10 for $[Co(9S3)_2][Ni(bdt)_2]_2$.

romagnetic interactions because of its small spin value. $[M(9S3)_2](TCNQ)_3$ (M = Ni, Co) are paramagnets, where partially reduced $TCNQ^{2/3-}$ molecules form a non-magnetic trimer which separates the $[Ni(9S3)_2]^{2+}$ cations from each other. The stacking of $(TCNQ)_3^{2-}$ trimers is disturbed by large $[M(9S3)_2]^{2+}$ cations, resulting in less conduction, in contrast to the typical highly conductive TCNQ salts. The five-coordinated complex $[Cu(9S3)Br_2]$ forms a 1D chain structure with strong intra-chain exchange interactions ($J = -5.4$ K) and weak inter-chain interactions. When we substitute a small amount of Cu^{2+} ion with Ni^{2+} ion, the arrangement of 1D AF chains changes drastically, and the distance of inter-chain S1–S3 contact decreases. The reduction of the inter-chain distance enhances two dimensionality, resulting in the onset of an AF transition at 4.5 K. $[Ni(9S3)_2][Ni(bdt)_2]_2$ is recognized by its cage-like structure, where the $[Ni(9S3)_2]^{2+}$ molecule is surrounded by two kinds of crystallographically independent $[Ni(bdt)_2]^-$ (A) and $[Ni(bdt)_2]^-$ (B) anions. $[Ni(9S3)_2]^{2+}$ and $[Ni(bdt)_2]^-$ (A) molecules form 1D FI chains, which are connected to each other by 1D chains of $[Ni(bdt)_2]^-$ (B) anions. The stacking of the planes of these cage-like structure causes competition between two kinds of inter-chain AF interactions between the FI chains. The competition brings about an WF transition at $T_N = 6.2$ K with an extraordinary large remanent magnetization $M_{REM} = 0.18$ μ_B, owing to the FI structure. Weak-ferromagnetism is also observed in the isostructural salt $[Co(9S3)_2][Ni(bdt)_2]_2$, although the remanent magnetization is small due to the absence of any ferrimagnetic structure. The origin of this weak-ferromagnetism is verified semi-quantitatively by a mean field calculation, where not only weak-ferromagnetism, but also the large M_{REM} of the $[Ni(9S3)_2]^{2+}$ salt and the small M_{REM} of the $[Co(9S3)_2]^{2+}$ salt are reproduced when competition between two kinds of AF interactions exists.

Finally, we emphasize the two important features of transition metal complexes with crown thioethers. One of the features is the presence of strong inter-molecular magnetic interactions through S–S atomic contacts owing to the characteristic electronic structure of crown thioethers. Indeed, some of the present samples have strong magnetic interactions (few to ca. −20 K) despite S–S contacts longer than the sum of the van der Waals radii. The other important feature is the substitutability between central transition metal ions having different spin states (for example, $S = 1$ component $[Ni(9S3)_2]^{2+}$ and $S = 1/2$ component $[Co(9S3)_2]^{2+}$). As the molecular sizes and structures remain unchanged by the substitution, chemical modification can be done intentionally in the systematic manner of tuning magnetism. From these features, it is concluded that the transition metal complexes of crown thioethers are promising building blocks in designing molecule-based magnets.

This work was supported by a Grant-in-Aid for Scientific Research No. 12046231, 15073211 and Grant-in-Aid for the 21st Century COE Program "Creation of Molecular Diversity and Development of Functionalities" from the Ministry of Education, Culture, Sports, Science and Technology. One of the authors (J. N.) was supported by a Grant-in-Aid for JSPS Fellows.

References

1 S. M. Holmes and G. S. Girolami, *J. Am. Chem. Soc.*, **121**, 5593 (1999).

2 J. S. Miller and A. J. Epstein, *Science*, **252**, 1415 (1991).

3 S. Ferlay, T. Mallah, R. Ouahès, P. Veillet, and M. Verdaguer, *Nature*, **378**, 701 (1995).

4 E. Dujardin, S. Ferlay, X. Phan, C. Desplanches, C. Cartier dit Moulin, P. Sainctavit, E. Baudelet, P. Veillet, and M. Verdaguer, *J. Am. Chem. Soc.*, **120**, 11347 (1998).

5 K. Falk, M. Balanda, Z. Tomkowicz, F. Mascarenhas, J. Schilling, P. Klavins, and W. Haase, *Polyhedron*, **20**, 1521 (2001).

6 T. Manabe, T. Kawashima, T. Ishii, H. Matsuzaka, M. Yamashita, T. Mitani, and H. Okamoto, *Synth. Met.*, **116**, 415 (2001).

7 T. Sugano, *Polyhedron*, **20**, 1285 (2001).
8 A. Caneschi, D. Gatteschi, N. Lalioti, C. Sangregorio, R. Sessoli, G. Venturi, A. Vindigni, A. Rettori, M. G. Pini, and M. A. Novak, *Angew. Chem., Int. Ed.*, **40**, 1760 (2001).
9 T. Enoki, J.-I. Yamaura, and A. Miyazaki, *Bull. Chem. Soc. Jpn.*, **70**, 2005 (1997).
10 A. Miyazaki, K. Enomoto, K. Okabe, H. Yamazaki, J. Nishijo, T. Enoki, E. Ogura, K. Ugawa, Y. Kuwatani, and M. Iyoda, *J. Solid State Chem.*, **168**, 547 (2002).
11 H. Kobayashi, A. Kobayashi, and P. Cassoux, *Chem. Soc. Rev.*, **29**, 325 (2000).
12 A. Sato, E. Ojima, H. Akutsu, Y. Nakazawa, H. Kobayashi, H. Tanaka, A. Kobayashi, and P. Cassoux, *Phys. Rev. B: Condens. Matter*, **61**, 111 (2000).
13 S. Uji, H. Shinagawa, T. Terashima, T. Yakabe, Y. Terai, M. Tokumoto, A. Kobayashi, H. Tanaka, and H. Kobayashi, *Nature*, **410**, 908 (2001).
14 N. Hanasaki, H. Tajima, M. Matsuda, T. Naito, and T. Inabe, *Phys. Rev. B: Condens. Matter*, **62**, 5839 (2000).
15 J. Nishijo, E. Ogura, J. Yamaura, A. Miyazaki, T. Enoki, T. Takano, Y. Kuwatani, and M. Iyoda, *Solid State Commun.*, **116**, 661 (2000).
16 E. Coronado, J. R. Galan-Mascaros, C. J. Gomez-Garcia, and V. Laukhin, *Nature*, **408**, 447 (2000).
17 F. Palacio, G. Antorrena, M. Castro, R. Burriel, J. Rawson, J. N. B. Smith, N. Bricklebank, J. Novoa, and C. Ritter, *Phys. Rev. Lett.*, **79**, 2336 (1997).
18 J. R. Hartman and S. R. Cooper, *J. Am. Chem. Soc.*, **108**, 1202 (1986).
19 N. Gallego-Planas and M. A. Whitehead, *J. Mol. Struct.: THEOCHEM*, **428**, 67 (1998).
20 T. W. Hambley, *Inorg. Chem.*, **37**, 3767 (1998).
21 A. J. Blake, M. J. Bywater, R. D. Crofts, A. M. Gibson, G. Reid, and M. Schröder, *J. Chem. Soc., Dalton Trans.*, **1996**, 2979.
22 J. P. Ferraris, D. O. Cowan, V. Walatka, Jr., and J. H. Prelstein, *J. Am. Chem. Soc.*, **95**, 948 (1973).
23 Y. Kagami, F. Iwahori, T. Ohishi, T. Hama, T. Manabe, M. Yamashita, H. Kitagawa, K. Sakai, and T. Mitani, *Synth. Met.*, **86**, 1803 (1997).
24 N. Gu, X.-M. Yang, H.-Y. Sheng, W. Lu, and Y. Wei, *Synth. Met.*, **71**, 2221 (1995).
25 W. N. Setzer, C. A. Ogle, G. S. Wilson, and R. S. Glass, *Inorg. Chem.*, **22**, 266 (1983).
26 M. J. Baker-Hawkes, E. Billig, and H. B. Gray, *J. Am. Chem. Soc.*, **88**, 4870 (1966).
27 G. Steimecke, H. Sieler, R. Kirmse, and E. Hoyer, *Phosphorus Sulfur Relat. Elem.*, **7**, 49 (1979).
28 E. Billing, R. Williams, I. Bernal, J. H. Waters, and H. B. Gray, *Inorg. Chem.*, **3**, 663 (1964).
29 J. Nishijo, A. Miyazaki, and T. Enoki, *Polyhedron*, **22**, 1755 (2003).
30 G. M. Sheldrick, "SHELXS86, program for crystal structure determination," Univ. of Göttingen, Federal Republic of Germany (1986).
31 G. M. Sheldrick, "SHELXL93, program for refinement of crystal structures," Univ. of Göttingen, Federal Republic of Germany (1993).
32 M. T. Azcondo, L. Ballester, S. Golhen, A. Guierrez, L. Ouahab, S. Yartsev, and P. Delhaes, *J. Mater. Chem.*, **9**, 1237 (1999).
33 T. Mori, A. Kobayashi, Y. Sasaki, H. Kobayashi, G. Saito, and H. Inokuchi, *Bull. Chem. Soc. Jpn.*, **57**, 627 (1984).
34 S. Flandrois and D. Chasseau, *Acta Crystallogr., Sect. B*, **33**, 2744 (1977).
35 G. J. Grant, C. G. Brandow, D. F. Galas, J. P. Davis, W. T. Pennington, E. J. Valente, and J. D. Zubkowski, *Polyhedron*, **20**, 3333 (2001).
36 J. J. Borrás-Almenar, E. Coronado, J. Curely, and R. Georges, *Inorg. Chem.*, **34**, 2699 (1995).
37 J. C. Bonner and M. E. Fisher, *Phys. Rev.*, **135**, A640 (1964).
38 D. B. Brown, J. A. Donner, J. W. Hall, S. R. Wilson, R. B. Wilson, D. J. Hodgson, and W. E. Hatfield, *Inorg. Chem.*, **18**, 2635 (1979).
39 I. Dzyaloshinskii, *Sov. Phys. JETP*, **5**, 1259 (1957); T. Moriya, *Phys. Rev.*, **120**, 91 (1960).
40 V. Skumryev, F. Ott, J. M. D. Coey, A. Anane, J.-P. Renard, L. Pinsard-Gaudart, and A. Revcolevschi, *Eur. Phys. J. B*, **11**, 401 (1999).
41 M. D. Lumsden, B. C. Sales, D. Mandrus, S. E. Nagler, and J. R. Thompson, *Phys. Rev. Lett.*, **86**, 159 (2001).
42 A. Miyazaki, K. Okabe, T. Enoki, F. Setifi, S. Golhen, L. Ouahab, T. Toita, and J. Yamada, *Synth. Met.*, **137**, 1195 (2003).
43 A. T. Coomber, D. Beljionne, R. H. Friend, J. L. Brédas, A. Charlton, N. Robertson, A. E. Underhill, M. Kurmoo, and P. Day, *Nature*, **380**, 144 (1996).
44 M. Drillon, E. Coronado, R. Georges, J. C. Gianduzzo, and J. Currely, *Phys. Rev. B: Condens. Matter*, **40**, 10992 (1989).
45 G. S. Wilson, D. D. Swanson, and R. S. Glass, *Inorg. Chem.*, **25**, 3827 (1986).